The Metallurgical and Mechanical Properties of ODS Alloy MA 956 Friction Welds

The influence of friction welding on the grain size and particle characteristics in completed joints was investigated

BY K. SHINOZAKI, C. Y. KANG, Y. C. KIM, M. ARITOSHI, T. H. NORTH AND Y. NAKAO

ABSTRACT. The metallurgical and mechanical properties of friction welded MA 956 oxide dispersion strengthened (ODS) iron-based superalloy material were investigated. The mechanical properties of friction welded joints were evaluated using a combination of room temperature and elevated temperature tensile testing and creep rupture testing. The microstructural features and particle characteristics were examined using optical and transmission electron microscopy. The distribution of residual stress in completed joints was analyzed using FEM analysis.

The room temperature and elevated temperature tensile strengths of friction welded joints were similar to those of as-received MA 956 base material and, in all cases, failure occurred away from the weld interface. However, the creep rupture properties of friction welded joints were much poorer than those of as-received MA 956 base material.

The friction welding operation created low-aspect-ratio, fully recrystallized grains at the joint centerline and substantially altered the oxide particle chemistry, dimensions and shape in the joint region. It is speculated that the coarse, irregularly shaped particles in regions immediately adjacent to the weld interface were produced as a result of a strain-induced agglomeration of small-diameter yttria dispersoids with larger-diameter alumina and Ti(C,N) particles.

Thermal elastic-plastic FEM modeling was used to analyze the residual stress generated by the friction welding operation. Close to the weld interface, the residual stress component perpendicular to the axial direction was much higher than the circumferential and radial direction components. However, its magnitude was less than the yield stress of the as-received MA 956 base material. The calculated results suggest that no plastic strain was produced as a direct result of cooling following friction welding.

K. SHINOZAKI is Associate Professor, Dept. of Mechanical Engineering, Hiroshima University, Hiroshima, Japan. C. Y. KANG is Associate Professor, Dept. of Metallurgical Engineering, Pusan University, Pusan, Korea. Y. C. KIM is Associate Professor, Japan Welding Research Institute, Osaka University, Osaka, Japan. M. ARITOSHI is Chief Researcher, Hyogo Prefectural Institute of Industrial Research, Hyogo, Japan. T. H. NORTH is Professor, Dept. of Metallurgy and Materials Science, University of Toronto, Toronto, Canada. The late Y. NAKAO was Professor, Dept. of Welding and Production Engineering, Osaka University, Osaka, Japan.

Introduction

Oxide Dispersion Strengthened (ODS) materials have superior mechanical and corrosion resistance at high temperatures compared to conventional superalloys. This readily explains the driving force for the replacement of wrought or cast superalloys by ODS materials for aerospace industry applications. Iron-based ODS superalloys comprise MA 956 (containing 20 wt-% Cr, 0.5 wt-% Y_2O_3) and MA 957 (containing 14 wt-% Cr, 0.25 wt-% Y_2O_3) and have higher melting points and improved corrosion resistance properties compared to nickel-based ODS alloys. The present paper investigates the properties of friction welded iron-based MA 956 superalloy base material.

Ideally, the mechanical properties of as-received ODS base material and the joint region should be identical; however, this has not proved to be the case. When ODS superalloys are joined using fusion welding, e.g., using gas tungsten arc, electron beam and laser beam welding, the completed joints have inferior creep rupture strengths at high temperatures compared to as-received ODS base material (Refs. 1–6). The inadequate creep rupture strength of fusion welded ODS base material has been associated with agglomeration of oxide dispersoids in the melt region and with the formation of fine-grained, dispersoid-free solidification structures that favor preferential damage accumulation. In addition, the mechanical properties of transient liquid phase (TLP) bonded ODS base material are inferior to that of as-received base material. For example, Nakao, *et al.* (Ref. 7), found that the creep rupture strengths of TLP-bonded MA 956 samples were poorer due to oxide segregation at the melt zone-base metal interfaces and nucleation of polycrystals in the melted region.

Limited research has been published indicating the detailed metallurgical changes that occur during friction welding of ODS superalloys. Moore, *et al.* (Ref. 8), compared the properties of friction welded joints in precipitation-hardened Udimet 700 and dispersion-strengthened TD-Ni superalloy materials. Udimet 700 friction joints had tensile and creep rupture strengths equivalent to the as-received base material. However, the creep rupture strength of TD-Ni joints at 1090°C were less than 10% of the as-received base material properties. The poor creep rupture strength of TD-Ni joints was ascribed to a combination of factors, *i.e.*, to the for-

KEY WORDS

MA 956 Superalloy
Oxide Disp. Strengthened
Friction Welding
FEM Modeling
Tensile Strength
Residual Stress
Yield Stress
Plastic Strain

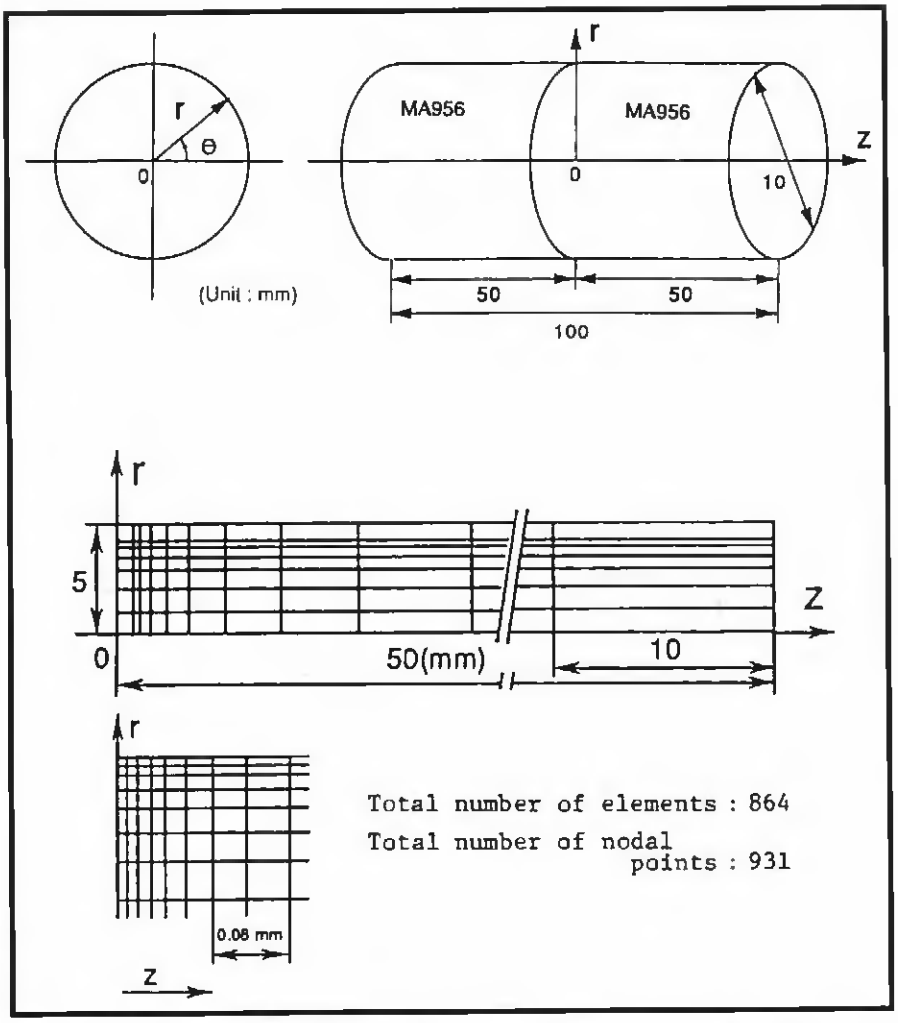

Fig. 1 — Component geometry, coordinate system and grid employed during FEM analysis of residual stress generation.

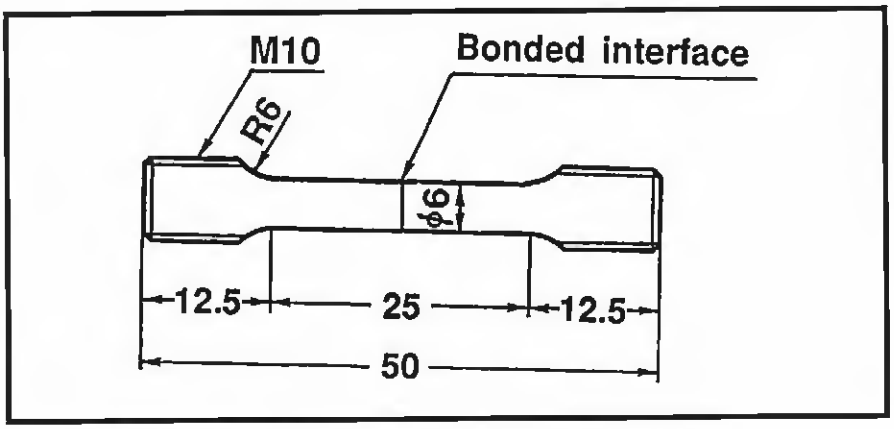

Fig. 2 — Design of the high-temperature tensile and creep test specimens.

Table 1 — Chemical Composition of MA 956 Base Material

Material	C	Mn	Si	Ni	Cr	Ti	Al	Y_2O_3	Fe
MA956	0.014	0.10	0.11	0.09	18.81	0.37	4.57	0.495	Bal.

mation of recrystallized grains at the joint centerline and segregation of oxide material at the weld interface promoted because of limited deformability of the base material (Ref. 8). Similarly, Jahnke, *et al.* (Ref. 5), suggested that limited deformability of the base material promoted retention of oxide material and contamination at the contact region of friction welded Ni-based superalloys containing high γ' contents.

The present paper presents the results of a comprehensive study of the metallurgical and mechanical properties of MA 956 friction welds. The following aspects are highlighted:

- The effect of joining parameter settings on tensile strength properties
- The influence of friction welding on the grain size and particle characteristics (diameter, shape, chemistry and area fraction) in completed joints
- Residual stress generation when the component cools to room temperature following friction welding
- The mechanical properties of friction welded joints (involving room temperature and high temperature tensile testing, and creep rupture testing).

Experimental

Materials

The chemical composition (in wt-%) of the MA 956 base material employed in the present study is shown in Table 1. This material was supplied as hot-extruded bars that were heat treated at 1273 K for 1 h. Test samples 10 mm in diameter x 50 mm long were prepared for friction welding experimentation with the long dimension parallel to the hot extrusion direction in the as-supplied MA 956 base material. Prior to friction joining, the contacting surfaces were polished using a lathe (the final surface finish was similar to that produced with #1200 grade emery paper) and cleaned using acetone.

Welding Parameter Settings

Friction welding was carried out using a direct-drive friction welding device. The following range of welding parameter settings was investigated:

- Friction Pressure: 20, 50 and 100 MPa
- Friction Time: 2, 5 and 8 s
- Forging Pressure: 20–250 MPa
- Forging Time: 6 s
- Rotation Speed: 2400 rpm

Table 2 shows the joining parameters investigated and the resulting ultimate tensile strength properties of as-welded MA 956 friction joints. Detailed micro-

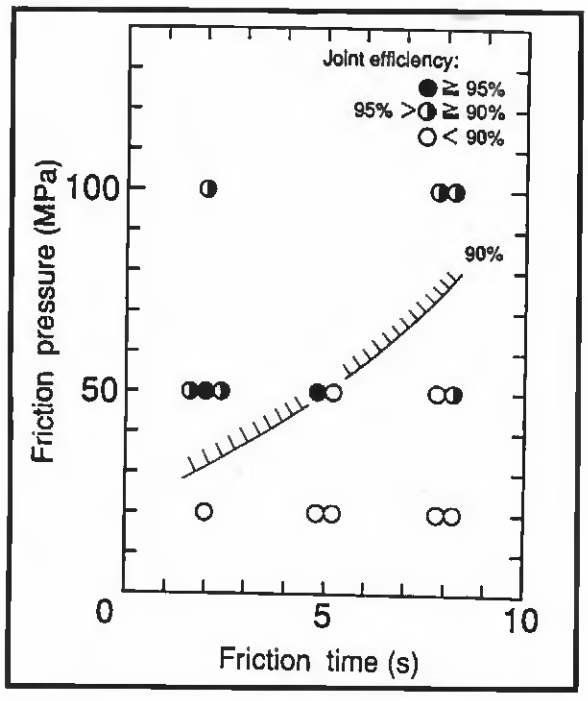

Fig. 3 — Effect of friction pressure and friction time on joint tensile strength properties (the joint efficiency is the ratio of the ultimate tensile strength of the joint and the as-received base material).

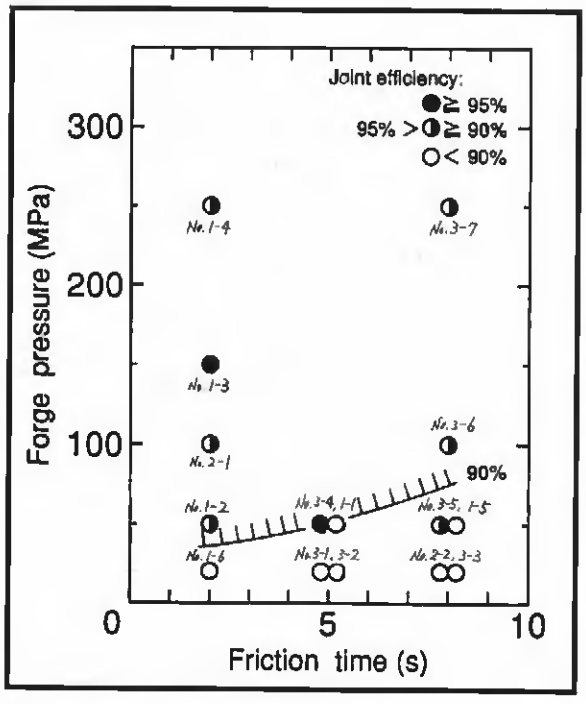

Fig. 4 — Effect of forging pressure and friction time on joint tensile strength properties (the joint efficiency is the ratio of the ultimate tensile strength of the joint and the as-received base material).

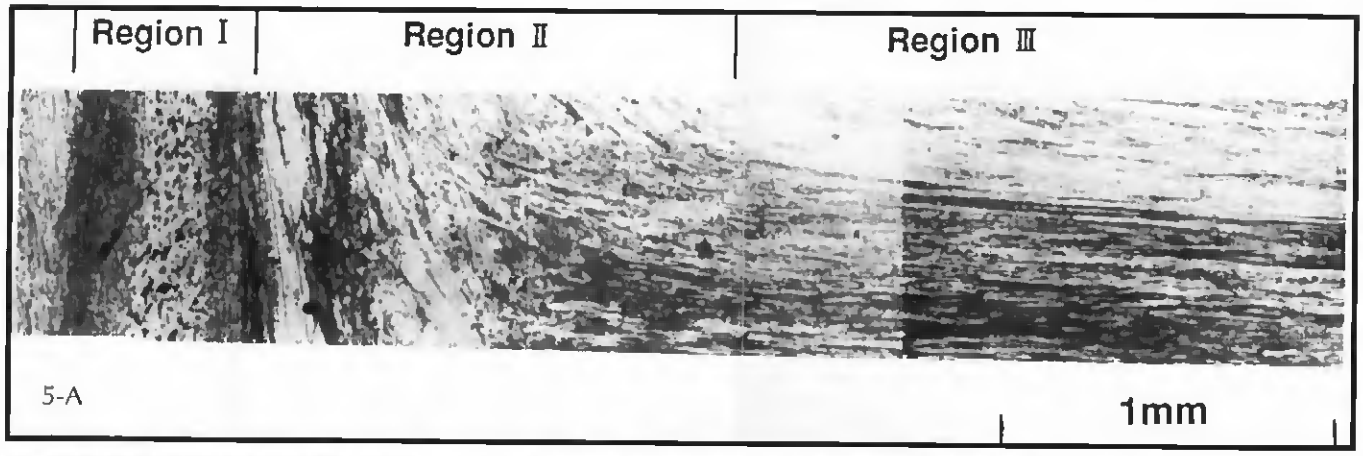

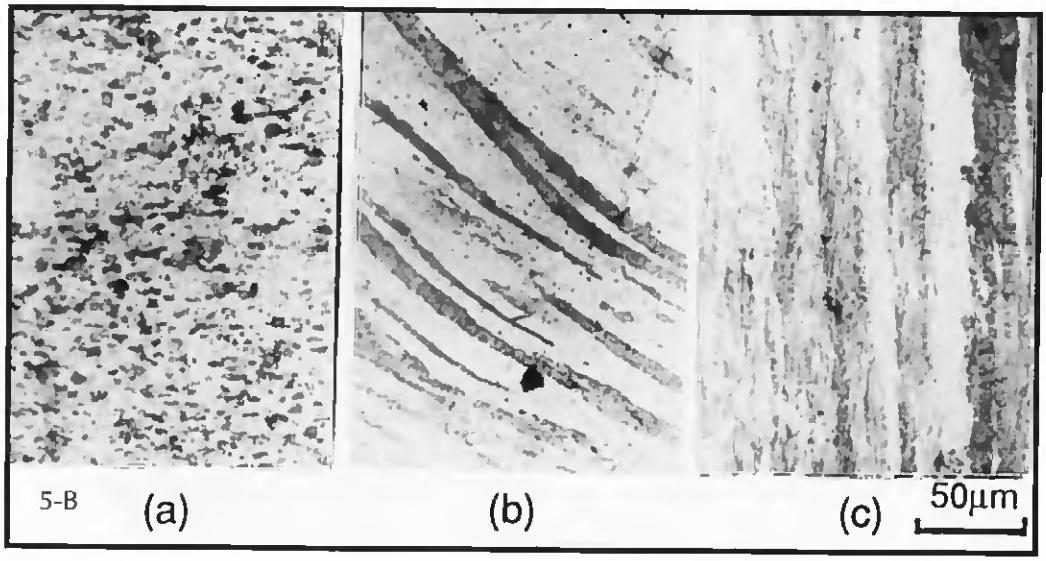

Fig. 5 — Friction welded MA 956 base material (at a friction pressure of 50 MPa, a forging pressure of 50 MPa, a friction welding time of 2 s and a forging time of 6 s). A — Regions RI, RII and RIII at low magnification; B — Regions RI, RII and RIII at high magnification.

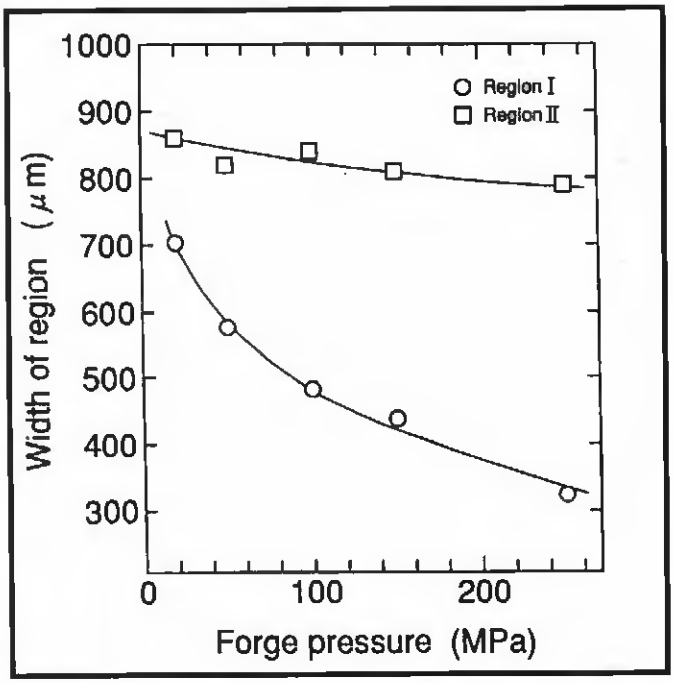

Fig. 6 — Influence of forging pressure on the width of regions RI and RII (measured at the component centerline). The reported values are the average of measurements taken at the component centerline and at ± 3 mm in the radial direction on either side of the component centerline.

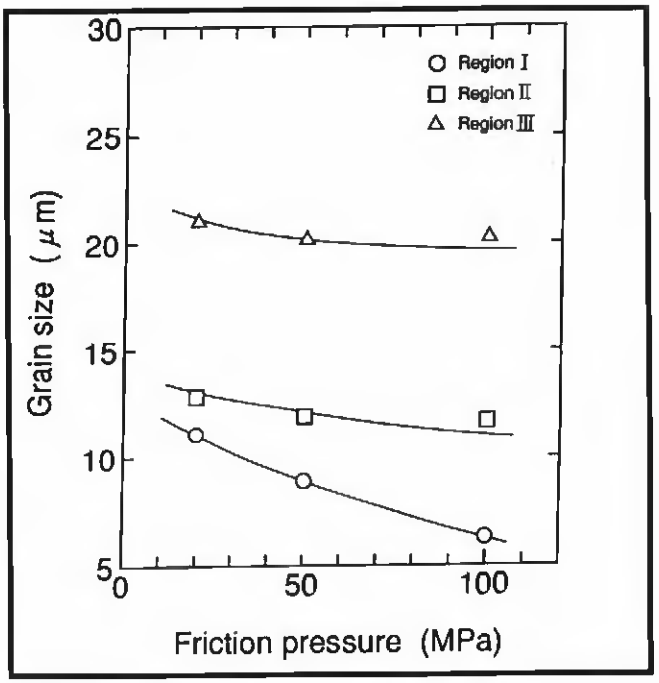

Fig. 7 — Influence of friction pressure on the average grain size in regions RI, RII and RIII. The reported values are the average of measurements taken at the component centerline and at ± 3 mm in the radial direction on either side of the component centerline.

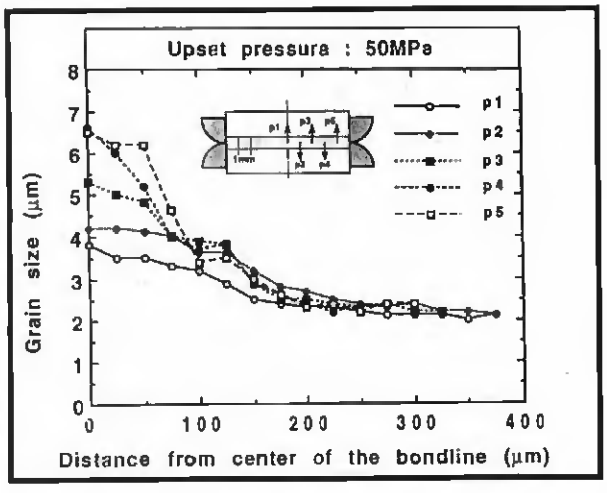

Fig. 8 — Variation in grain size in the region very close to the weld interface for different radial distances (in a joint completed using a friction pressure of 50 MPa and a forging pressure of 50 MPa). Locations p1, p2, p3, p4 and p5 are 1 mm apart.

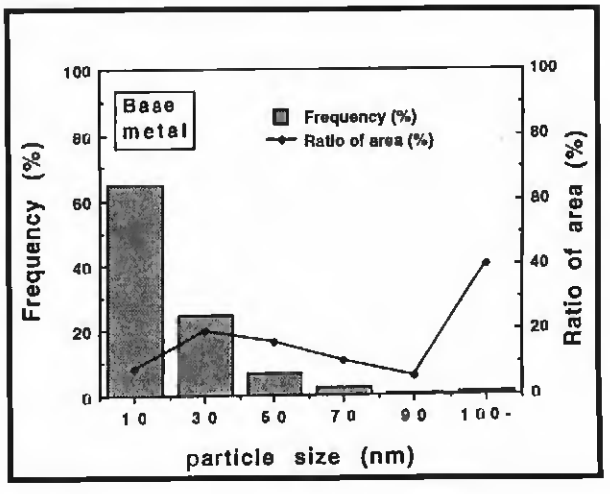

Fig. 9 — Particle size distribution in the as-received MA 956 base material.

scopic analysis was carried out on MA 956 joints produced using a friction welding pressure of 50 MPa, a friction time of 2 s and forging pressures of either 50 or 150 MPa (each applied for a holding time of 2 s).

Metallography

Both optical and electron microscopy were employed to characterize the friction welded test specimens. Samples for optical metallography were prepared by sectioning the welded joint at right angles to the weld interface along the diameter. The test samples were electropolished and etched in a solution of 5 vol-% HCl and 95 vol-% ethanol. Transmission electron microscopy (TEM) samples were prepared as follows. Test specimens (0.5–1.0 mm thick) were carefully extracted by sectioning perpendicular to the weld interface and mechanically thinned to a thickness of 0.1–0.2 mm. The TEM foils were then polished and etched in a solution of 10 vol-% HCl and 90 vol-% ethanol so that a specific dimple location relative to the weld interface could be evaluated. The 3-mm-diameter dimpled foils were then electropolished with a twin-jet polisher (Struers-Tenupol) using a solution of 10 vol-% perchloric acid and 90 vol-% acetic acid. TEM imaging and energy-dispersive x-ray (ED5) analyses were carried out using a Hitachi H-800/8010 TEM/STEM micro-

scope operating at 200 kV.

The dimensions and area fraction of second-phase particles in a given size range in the base material and joint region were evaluated using point counting, *i.e.*, by examining 20 fields of view on micrographs taken at 5000X and 30,000X magnification on a range of test specimens. It must be borne in mind that there is an inherent error in this measurement approach because the TEM images are not two-dimensional in form and that this is especially the case when the particle dimensions are smaller than the foil thickness. With this in mind, the dimensional and area fraction measurements should be regarded as approximate indications of these parameters. The grain size was measured from TEM microsections extracted from five different locations at the joint interface (at the component centerline and in four sample locations at 1-mm distances from the centerline). The grain size was measured using the linear intercept method on two welded joints produced using identical joining parameter settings. Four photomicrographs were taken at 3000X magnification at each location during the analysis.

FEM Modeling of Residual Stress

The temperature dependency of the thermophysical constants (density, thermal expansion coefficient, thermal conductivity, specific heat) and the mechanical properties (elastic modulus, yield stress, ultimate strength) of MA 956 base material are shown in the Appendix — Figs. A1–A3. Although axial shortening occurred during friction welding, this has no influence on residual stress generation because MA 956 base material has very low yield strength at temperatures exceeding 1473 K. Because the yield strength of MA 956 base material is low (50 MPa) at temperatures above 1473 K only plastic deformation results from the forging operation. Residual stress is generated when the joint cools from 1473 K to room temperature. It will be shown that the magnitude of the calculated residual stress values is much less than the yield strength of the MA 956 base material at room temperature (700 MPa) and therefore it can be anticipated that no plastic straining occurs as a direct result of cooling from 1473 K to room temperature.

Figure 1 shows the component geometry, coordinate system and grid employed during FEM analysis. Isoparametric four-node finite elements were examined during the FEM analysis; the total number of elements was 864 and the total number of nodal points was 931.

Table 2—The Effect of Joining Parameters on the Ultimate Tensile Strength of MA 956 Joints

Rotation Speed (rpm)	Friction Pressure (MPa)	Forging Pressure (MPa)	Friction Time (s)	Forging Time (s)	Ultimate Tensile Strength (MPa)
2400	50	50	5	6	717
2400	50	50	2	6	774
2400	50	150	2	6	795
2400	50	250	2	6	784
2400	50	50	8	6	740
2400	20	20	2	6	645
2400	100	100	2	6	774
2400	20	20	8	6	542
2400	20	20	5	6	609
2400	20	20	5	6	628
2400	20	20	8	6	601
2400	50	50	5	6	804
2400	50	50	8	6	779
2400	100	10	8	6	785
2400	100	250	8	6	775

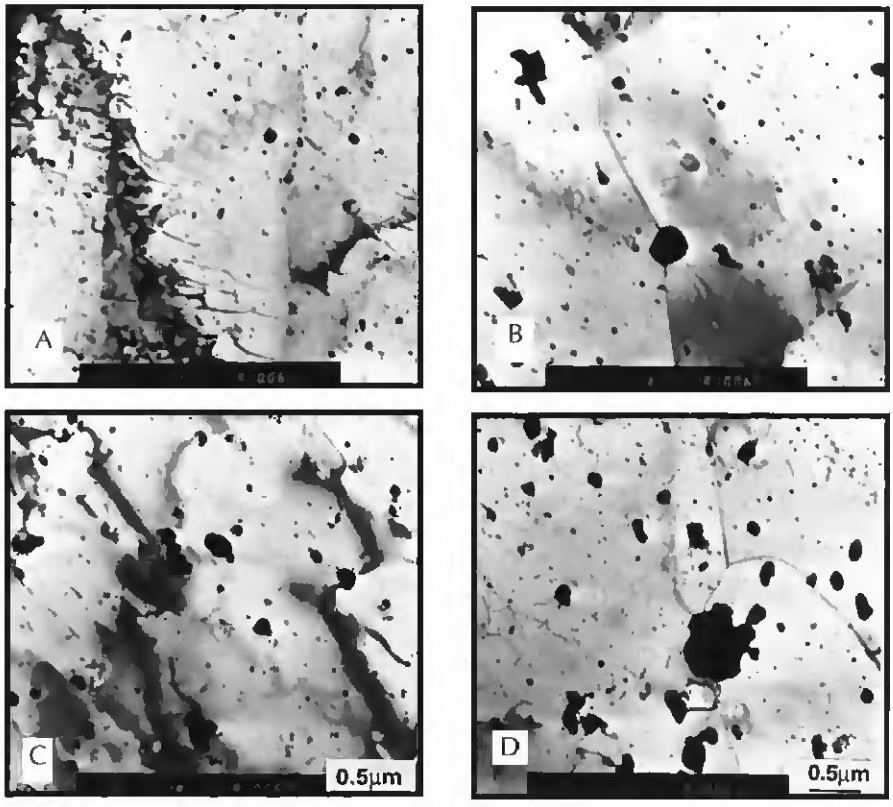

Fig. 10 — TEM micrographs showing the change in particle characteristics in regions of the joint. A — Region RIII; B — region RII; C — RIin is the joint centerline; and D — RIout is the boundary between regions RI and RII.

The thermal history produced by the friction welding operation was calculated using an unsteady-state, axisymmetric, thermal conduction FEM analysis. In these calculations, the heat generated, q, during welding was 1.39 kJ/s and this energy was generated in a 2-s friction welding period. This FEM modeling approach has already provided an excellent correlation between experimentally measured and calculated results during dissimilar friction joining of titanium and AISI 304L stainless steel (Ref. 11). The calculated peak temperature during friction welding of MA 956 base material was compared with that measured using two-color pyrometry. It is worth noting that two-color pyrometry only indicates the temperature attained at the joint periphery. It should be noted in all figures that the distance noted is the distance from the final weld interface location.

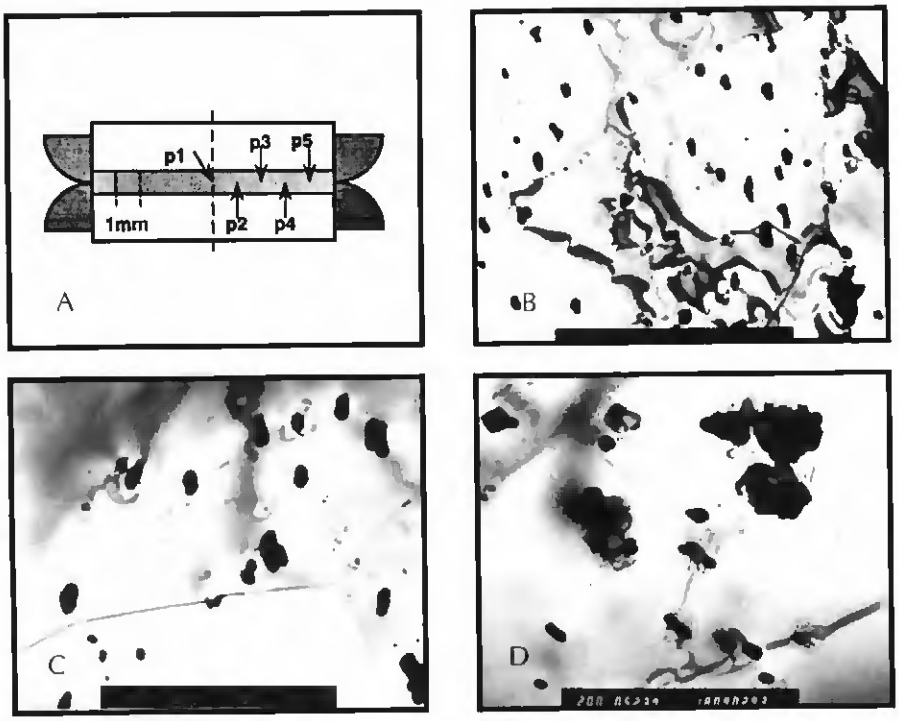

Fig. 11 — Coarse, irregularly shaped particles found at different radial distances in region RI. Locations p1, p3 and p5 are 2 mm apart. A — Schematic of particle locations; B — p1; C — p3; and D — p5.

Table 3A — The Relative Frequencies and Average Diameters of Particles Having Dimensions Exceeding 100 nm in the As-Received MA 956 Base Material

	Al	Ti	Y-Al	Al-Y	Al-Ti	Y-Al-Ti
F[a] (%)	13	50	21	8	4	4
d[b] (nm)	480	330	260	280	400	320

(a) F = Frquency (%)
(b) d = Average Diameter
(c) Number of particles measured = 200.

Table 3B — The Relative Frequencies and Average Diameters of 200 Particles Observed at the Weld Interface in Friction Welded MA 956 Base Material at a Forging Pressure of 50 MPa

	Y-Al	Ti	Al-Ti	Al-Y	Y-Al-Ti	Mix[c]
F[a] (%)	61.8	5.9	1.4	1.4	8.8	20.7
d[b] (nm)	360	210	320	180	480	640

(a) F = Frequency (%)
(b) d = Average diameter
(c) Number of particle measured = 200.
Note: For Tables 3A and 3B, Al refers to aluminum-rich particles; Ti refers to titanium-rich particles; Y-Al refers to yttrium-rich particles containing aluminum; Al-Y refers to aluminum-rich particles containing yttrium; Al-Ti refers to aluminum-rich particles containing titanium; and Y-Al-Ti refers to yttrium-rich particles containing aluminum and titanium. Mix refers to particles that contain a mixture of yttrium, titanium and aluminum.

Mechanical Properties

The mechanical properties of friction welded MA 956 base material were evaluated using a combination of room temperature and elevated temperature tensile testing and creep testing. The ultimate tensile strength (at room temperature) of the MA 956 base material was 835.5 MPa. The dimensions of the tensile test samples were 6 mm diameter x 50 mm long. High-temperature tensile testing was carried out in an argon atmosphere at 923 K. During room temperature tensile testing, the crosshead speed was 0.017 mm/s. During high-temperature tensile testing, the crosshead speed was 0.37 mm/s. The holding time at temperature was 300 s prior to testing. In subsequent figures, the ultimate tensile strengths of completed joints are reported.

The creep rupture properties of MA 956 friction joints were evaluated at 923 K (the applied stress was 880 MPa during testing). The creep rupture test specimen dimensions were also 6 mm diameter x 50 mm long — Fig. 2. During high-temperature tensile and creep testing, the test specimens were induction heated at 0.15 K/s from room temperature to 923 K.

Results and Discussion

Joining Parameters and Mechanical Properties

Figures 3 and 4 show the effects of friction pressure, friction time and forging pressure on the room temperature tensile strength properties of MA 956 friction welds. Table 2 shows a detailed breakdown of the joining parameter settings applied and the resulting joint mechanical properties. In these figures, the influence of different joining parameter settings on joint efficiency is shown graphically (the joint efficiency is the ratio of the ultimate tensile strengths of the joint and the MA 956 base material).

Grain Size Variation

The different regions in the friction welded joint are shown in Fig. 5A and B. For convenience, the friction welded joint is subdivided into discrete microstructural regions:

Region RI: the fully plasticized region on either side of the weld interface. This region contains small equiaxed recrystallized grains and has a "single lens" shape (like a double convex lens).

Region RII: the region where the base material grains are plastically deformed by the forging cycle that completes the friction welding operation. This region has a "single lens" shape (like a double convex lens).

Region RIII: the as-received base material comprising elongated grains oriented parallel to the extrusion direction.

Figure 6 shows the influence of forging pressure on the width of regions RI and RII. The reported values are the *average* of measurements at the component centerline and at ± 3 mm in the radial direction on either side of the component centerline. The dimensions of regions RI and RII both decreased when the forging pressure increased from 20 to 250 MPa.

The influence of friction pressure on the average grain size in regions RI and RII is shown in Fig. 7. An increase in friction pressure markedly decreased the average grain size in region RI. Increasing friction pressure also decreased the grain size in region RII.

Figure 8 shows the change in grain size across region RI (the region close to the joint interface). The grain size was largest at the weld interface and, in the axial direction, decreased when traversing region RI. In the radial direction, the grain size markedly increased with in-

creasing distance from the component centerline — Fig. 8.

The formation of equiaxed grains in region RI is determined by the process of dynamic recrystallization. Increasing the temperature or lowering the strain rate at any location will result in larger subgrain dimensions (Ref. 9). The highest temperature occurs at the weld interface region and, consequently, this is where the largest grain size was observed for any given radial location — Fig. 8. The presence of finer grain size in areas away from the weld interface (at the RI/RII boundary) is consistent with the lower temperatures and strains that occur in this location. Based on a first order assumption that a constant pressure distribution and constant effective frictional coefficient are applied during friction joining, higher temperatures may be produced close to the joint periphery. Although this might explain the larger grain size observed at increasing radial distances, it is worth noting that the pressure distribution is not uniform when joining solid bars and the effective frictional coefficient is not constant.

Particle Characteristics

Figure 9 shows the particle size distribution and the area fraction of particles in the as-received MA 956 base material. Many oxide particles in the superalloy base material had dimensions less than 20 nm. Table 3A shows the average diameter and chemical compositions of 200 particles having dimensions exceeding 100 nm in the MA 956 base material. Based on a detailed comparison with published research on particles detected in MA 956 base material (where both X-ray diffraction (XRD) and energy dispersive (EDS) analyses were applied), it is estimated qualitatively that the large (>100-nm-diameter) particles that exhibited Al only and Ti only were Al_2O_3 and Ti(C,N), respectively (Ref. 10). Particles displaying Y-Al peaks during EDS analysis were oxide mixtures of Y_2O_3 and Al_2O_3 while those displaying Al-Ti and Y-Al-Ti peaks comprised mixtures of different oxides or oxide and carbo-nitride species.

Figure 10 shows the qualitative changes in the dimensions and shapes of particles observed in regions RI, RII and RIII of the joint. Many coarse and irregularly shaped particles were observed in regions RI and RII. The size of the irregularly shaped particles observed in region RI markedly increased near the joint periphery — Fig. 11. In addition, the chemical composition varied across coarse irregularly shaped particles — Fig. 12. For example, in Fig. 12, location A is rich in Al and Y and location B is rich in Ti, while the central region of the particle contains a mixture of Y, Al and Ti.

Tables 3A and B compare the average diameters and chemical compositions of 200 particles having diameters >100 nm in region RI with those found in the as-received base material. It is important to note that particle agglomeration substantially altered the number and distribution of the small-diameter yttria particles observed in the joint region.

It has been speculated that the combination of plastic flow, possibly in conjunction with locally melted regions at grain boundaries in the MA 956 base material, promotes agglomeration of small yttria particles with larger alumina and Ti(C,N) particles (Ref. 10). Following agglomeration, chemical reaction occurs between yttria and alumina and, during cooling, the shape of the agglomerated particles is determined by the driving force to decrease the particle/matrix interfacial energy. Figure 13 shows a schematic representation of this particle agglomeration mechanism. The shape of the irregularly shaped particles in Figs. 10–12 and the variation in chemical composition across irregularly shaped particles (Fig. 12) are consistent with the proposed particle agglomeration mechanism.

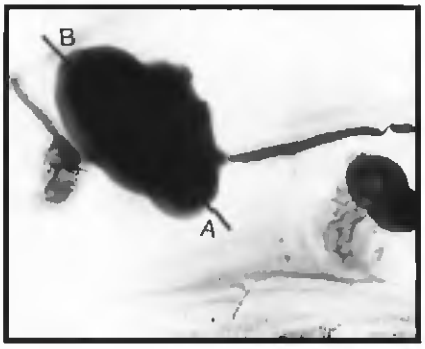

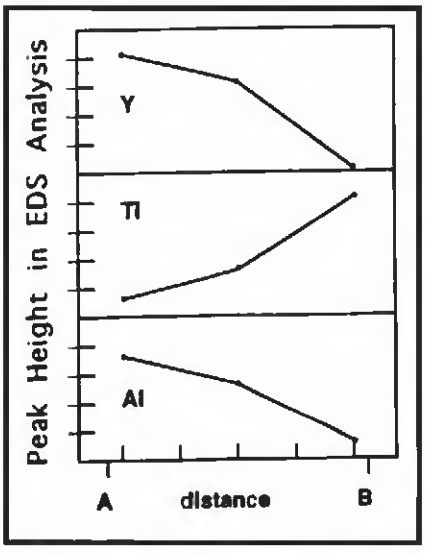

Fig. 12 — Variation in chemical composition (the variation in peak height during EDS analysis) along the length of a coarse particle.

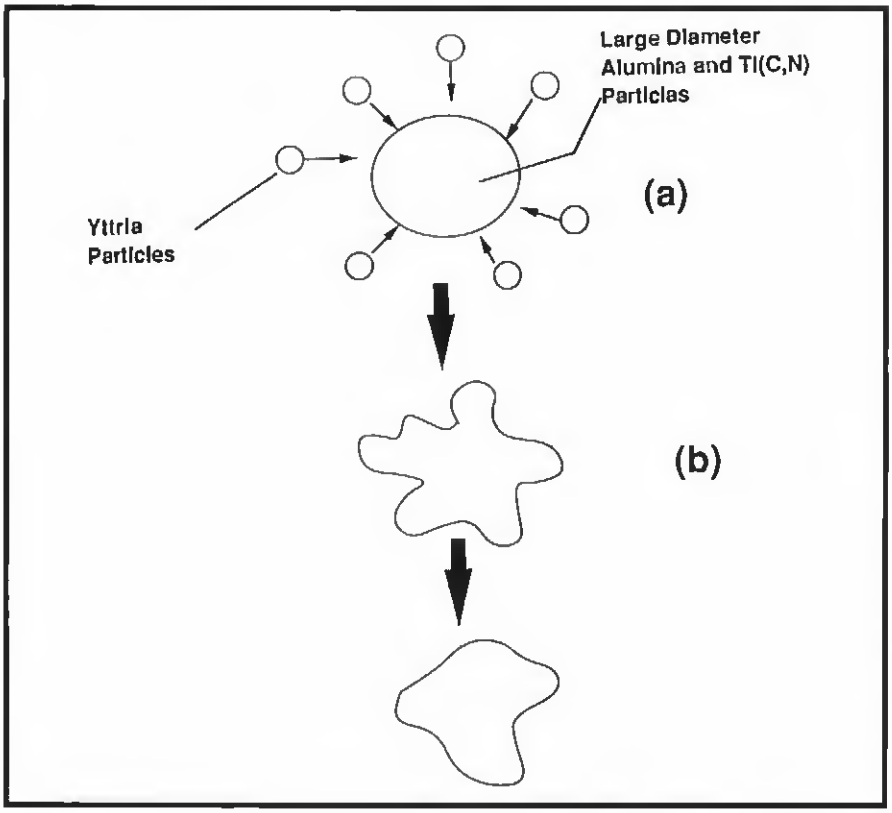

Fig. 13 — Possible particle agglomeration mechanism (after Ref. 10).

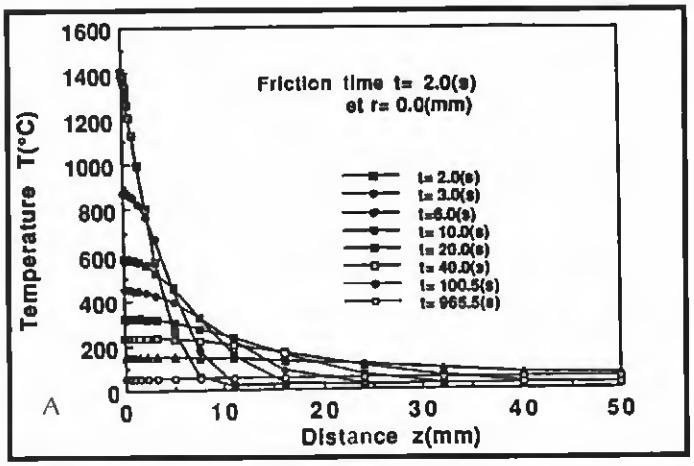

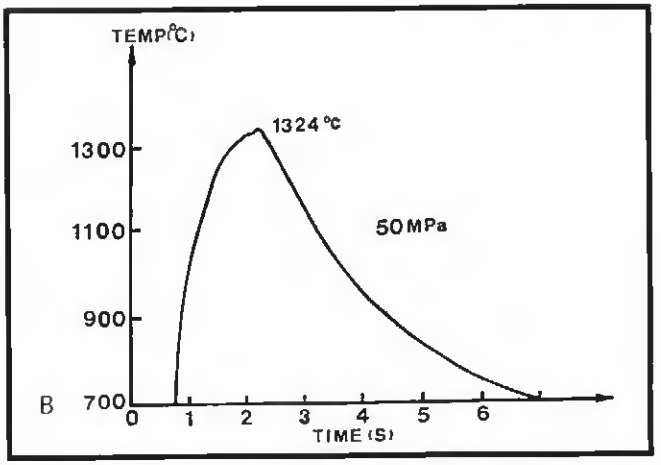

Fig. 14 — A — Calculated thermal cycle at the joint centerline; B — thermal cycle at the joint periphery (measured using optical pyrometry).

Residual Stress

The calculated temperature distribution produced in the z-direction at the component centerline is shown in Fig. 14A. The experimentally measured temperature cycle at the joint periphery is shown in Fig. 14B. The calculated and experimentally measured peak temperature values were 1673 and 1597 K, respectively. Using the calculated thermal history, residual stress generation was examined via an axisymmetric, thermal elastic-plastic stress analysis (assuming the Von Mises criterion).

Figure 15A–C shows the distributions of σ_z (perpendicular to the weld interface), σ_r (radial direction) and σ_θ (circumferential direction) as a function of radial distance from the component centerline in the region immediately adjacent to the joint interface. σ_z is tensile across much of the radius and becomes compressive near the joint periphery. The behavior of σ_θ in the radial direction is similar to that of σ_z. In contrast, σ_r has a small tensile value across the radius. In the radial direction, σ_z is much higher than σ_r or σ_θ.

Because σ_z has a large influence on final joint strength, the σ_z distribution in the axial direction will be discussed in more detail. Figure 16A and B shows the distribution of σ_z in the axial direction in the region close to the center of the component (at r = 0.5 mm) and close to the periphery of the joint (at r = 4.995 mm). Near the centerline, σ_z is tensile and becomes compressive in the region about 7 mm from the joint interface — Fig. 16A. The maximum tensile stress $(\sigma_z)_{max}$ occurs very close to the weld interface. Quite

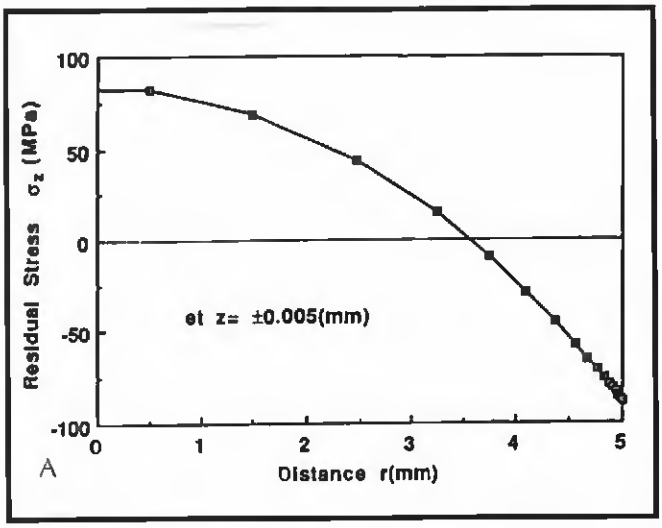

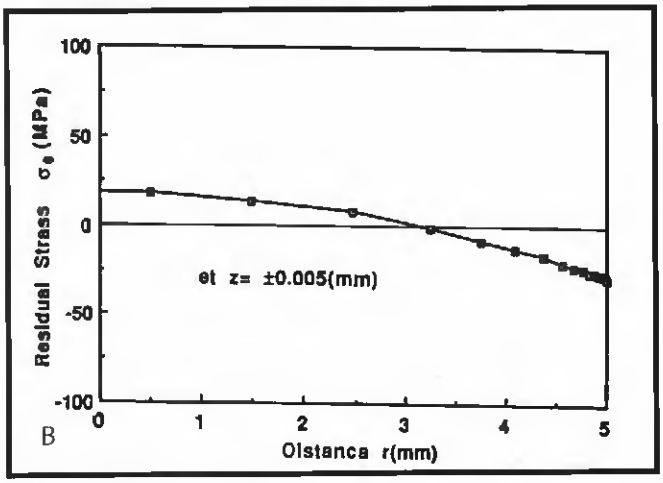

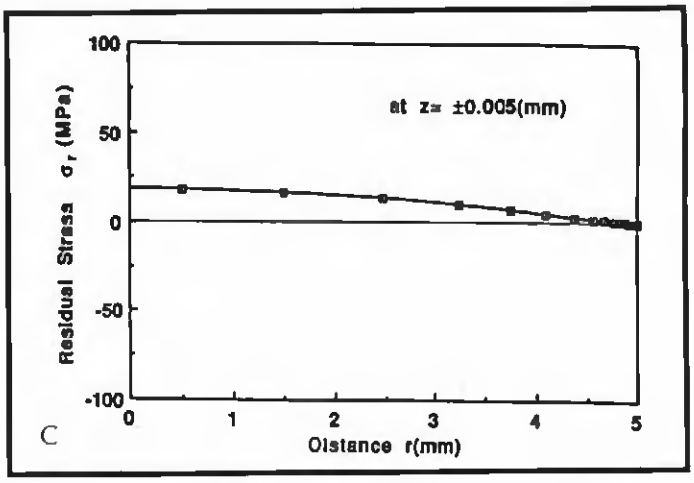

Fig. 15 — A — Distribution of σ_z in the radial direction (immediately adjacent to the weld interface); B — distribution of σ_θ in the radial direction (immediately adjacent to the weld interface); C — distribution of σ_r in the radial direction (immediately adjacent to the weld interface).

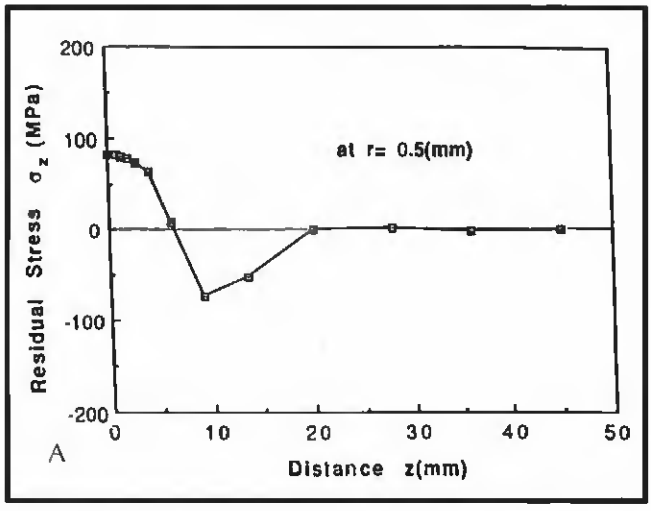

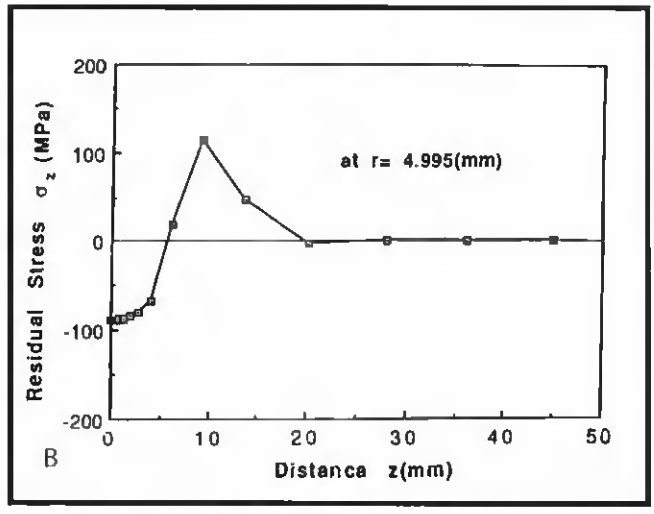

Fig. 16 — A — Distribution of σ_z in the direction perpendicular to the weld interface (close to the center of the component); B — distribution of σ_z in the direction perpendicular to the weld interface (close to the joint periphery).

different behavior was exhibited near the joint periphery — Fig. 16B. σ_z is compressive in the region close to the weld interface and becomes tensile in the region about 6 mm from the joint interface. The σ_z value has an important influence on the tensile strength of completed joints and the presence of compressive σ_z values at the joint periphery will have a beneficial effect on joint mechanical properties.

Figure 17 shows the distribution of σ_θ in the axial direction in the region close to the joint periphery (at r = 4.995 mm). The highest tensile values of σ_θ occur at a distance of 6 mm from the joint interface, σ_θ becomes compressive at about 4 mm from the joint interface.

The magnitudes of the calculated residual stress values are much less than the yield strength of the MA 956 base material at room temperature (700 MPa). Consequently, it can be anticipated that no plastic straining occurs as a direct result of cooling from 1473 K to room temperature.

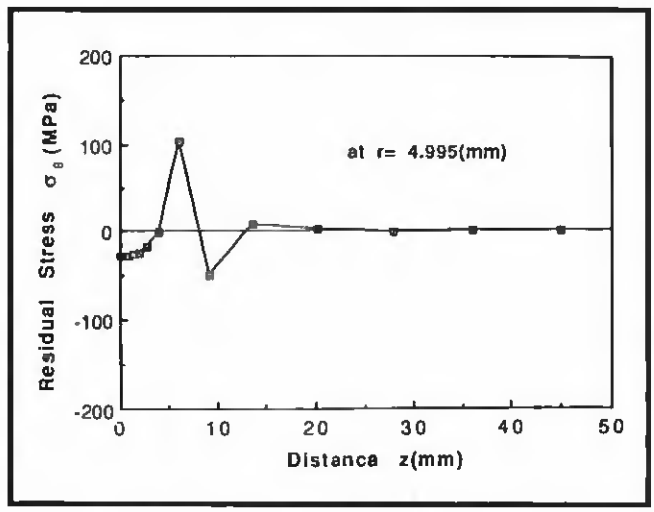

Fig. 17 — Distribution of σ_θ in the direction perpendicular to the weld interface (close to the periphery of the component).

Mechanical Properties

Figure 18A and B shows the tensile strength, elongation and reduction of area values of the welded test samples during room temperature and elevated temperature tensile testing (for forging pressures of 50 and 150 MPa, respectively). The friction welded joints had room tensile strength properties comparable to those of the as-received MA 956 base material. Also, detailed fractography confirmed that failure occurred away from the weld interface in all tensile test specimens.

Figure 19 compares the creep rupture properties of friction welded specimens with those of the base material tested in the longitudinal and transverse directions. The creep rupture life of friction welded joints was markedly poorer (about 10%) than that of the as-received MA 956 base material. When a forging pressure of 50 MPa was employed, fracture initiated in regions RI and RII and at the RI/RII boundary. In contrast, when a forging pressure of 150 MPa was employed during friction welding, fracture initiated in region RII. It is worth noting that many grain boundaries in region RII lie at 45 deg to the tensile axis and hence are aligned with the maximum resolved shear stress. This will facilitate grain boundary sliding and may, in part, account for the much lower creep rupture strength properties of MA 956 friction welded joints.

It is apparent that room temperature and elevated temperature tensile testing of friction welded MA 956 base material does not provide an effective indication of the likely creep rupture properties of completed joints. The friction welding operation creates low-aspect-ratio, recrystallized grains at the joint centerline, and substantially alters the oxide particle chemistry, dimensions and shape. The formation of low-aspect-ratio, recrystallized grains and the agglomeration of small-diameter yttria particles forming coarse, irregularly shaped oxide particles in the joint region readily accounts for the poor stress rupture properties and for preferential creep failure in region RI of friction welds produced using a forging pressure of 50 MPa. However, as mentioned earlier, the fracture location was preferentially located in region RII in friction welds produced using a forging pressure of 150 MPa. The results in Fig. 6 confirm that increasing forging pressure decreases the width of region RII. It has already been confirmed that the creep rupture strength is markedly decreased when the grain orientation favors preferential damage accumulation at grain boundary regions (Ref. 12). In joints produced using a forging pressure of 150 MPa it is suggested that many grains in

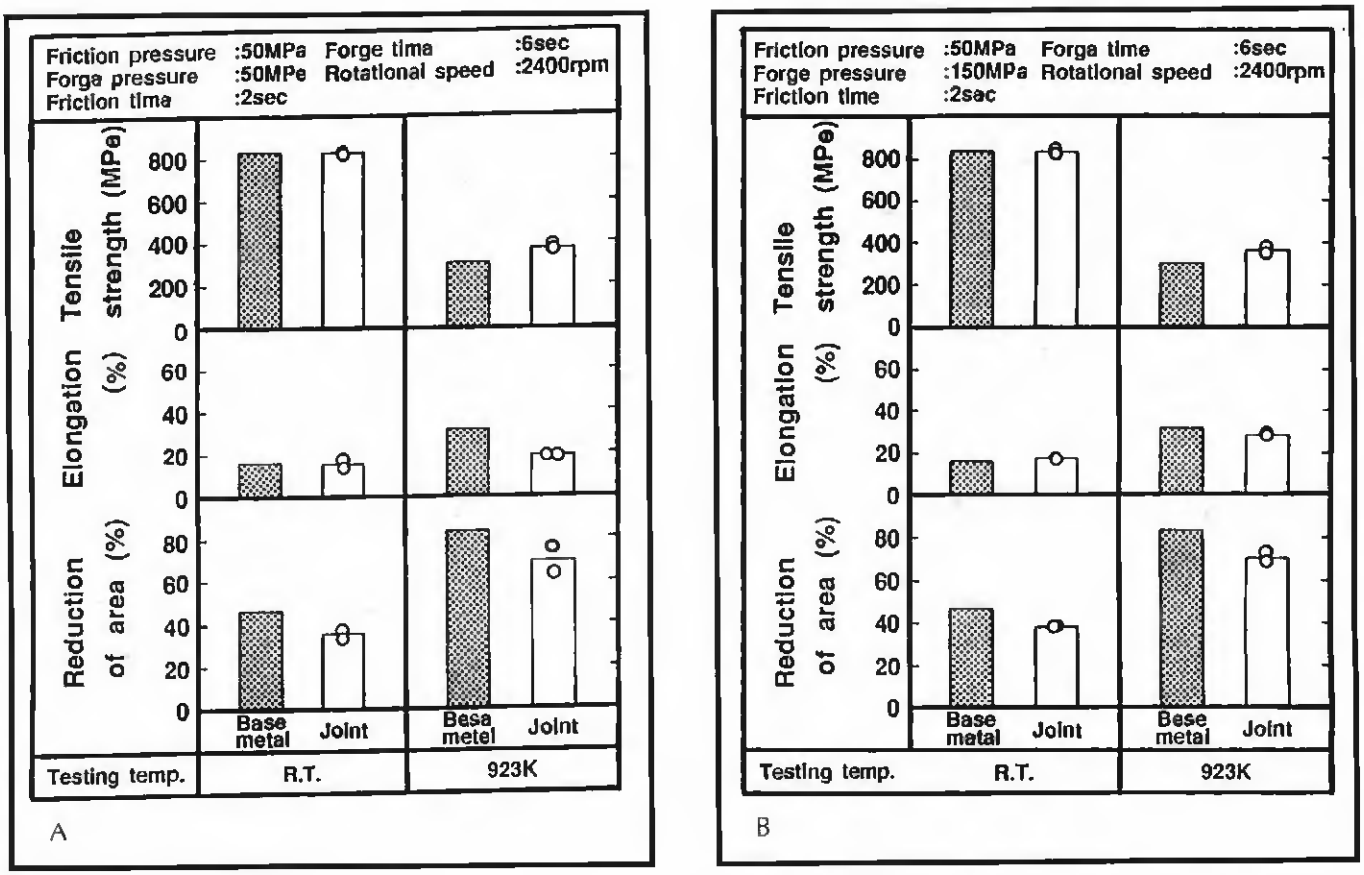

Fig. 18 — Room temperature and elevated temperature tensile strength properties. A — For a forging pressure of 50 MPa; B — for a forging pressure of 150 MPa.

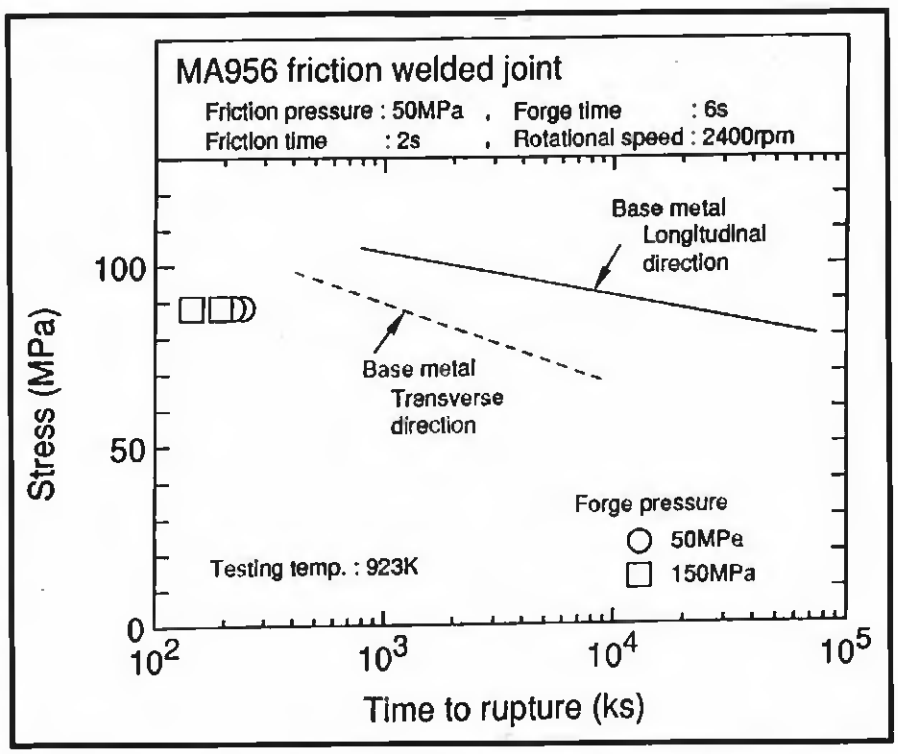

Fig. 19 — Creep rupture strength of friction welded MA 956 base material.

region RII become aligned so that preferential damage accumulation is promoted at grain boundary regions.

Conclusions

The metallurgical and mechanical properties of friction welded MA 956 superalloy base material were investigated. For convenience, the joints were considered to comprise three distinct regions: region RI, where fully recrystallized grains were observed; region RII, where the base material grains were deformed by the forging operation that completes friction welding; and the as-received MA 956 base material (region RIII). The following are the principal conclusions:

1) The room temperature and elevated temperature tensile strengths of friction welded joints were similar to those of as-received MA 956 base material.

2) The creep rupture properties of friction welded joints were much poorer than those of as-received MA 956 base material. The location of failure during creep rupture testing depended on the forging pressure applied during friction welding. Creep failure occurred in regions RI and RII and at the RI/RII bound-

ary in welds produced using a forging pressure of 50 MPa. When the forging pressure increased to 150 MPa, creep failure initiated in region RII. In joints produced using a higher forging pressure it is suggested that many grains become aligned so that preferential damage accumulation is promoted at grain boundary regions.

3) The friction welding operation created low-aspect-ratio, fully recrystallized grains at the joint centerline and substantially altered the oxide particle chemistry, dimensions and shape in the joint region. Coarse, irregularly shaped particles were observed in regions RI and RII adjacent to the weld interface. In region RI, it is speculated that the irregularly shaped oxide particles resulted from strain-induced agglomeration of small-diameter yttria dispersoids with larger-diameter alumina and Ti(C,N) particles.

4) Thermal elastic-plastic FEM modeling was used to analyze the residual stress generated hy the friction welding operation. Close to the weld interface in the radial direction, σ_z (the stress component in the axial direction) has a much higher value than σ_θ (the circumferential component) or σ_r (the radial component). The calculated results suggest that no plastic strain was produced as a direct result of cooling following the friction welding operation.

Acknowledgments

This joint research program was carried out by researchers working in the Department of Welding and Production Engineering, Osaka University, at the Japan Welding Research Institute, Osaka, and in the Department of Metallurgy and Materials Science, University of Toronto, Toronto, Ontario, Canada.

Professor Shinozaki would like to thank Mr. K. Oki, undergraduate student in the Department of Welding and Production Engineering, Osaka University, for his help during the experimentation.

Professors North and Kang would like to thank the Ontario Center for Materials Research for financial support for the portion of this research effort that was carried out at the University of Toronto.

Finally, the authors would like to acknowledge their debt to the late Professor Nakao for his guidance, constancy and fellowship during this work effort.

References

1. Kelly, T. J. 1981. Joining of oxide dispersion strengthened alloys. *Proc. Conf. on Frontiers of High Temperature Materials 1*, pp. 111. Inco Alloys International, New York, N.Y.

2. Kelly, T. J. 1979. Pulsed YAG laser welding of ODS alloys, *Proc. Conf. on Applications of Lasers in Materials Processing*, pp. 43. ASM International, Materials Park, Ohio.

3. Kelly, T. J. 1982. Brazing of Inconel Alloy 754 for high-temperature applications. *Welding Journal* 61(10)(: 317-s to 319-s.

4. Holko, K. H. 1973 An improved diffusion welding technique for TD NiCr sheet, *Welding Journal* 53(11): 515-s to 523-s.

5. Jahnke, B., and Dannhauser, G. 1984. Joining of superalloys, a summary and evaluation of work done within the Cost 50 III and Cost 501 programs. COST 501, Project D 39, Interim Report 2.

6. Molian, P. A., Yang, Y. M., and Patnaik, P. C. 1992. Laser welding of oxide dispersion strengthened MA 754. *J. Mat. Sci.*, 27: 2687–2694.

7. Nakao, Y., and Shinozaki, K. 1995. Transient liquid diffusion bonding of iron-based oxide dispersion strengthened alloy MA 956. *Mat. Sci. and Tech* 11(3): 304–311.

8. Moore, T. J. 1972 Friction welding Udimet 700. *Welding Journal* 47(4): 253–261.

9. Midling, O. T., and Grong, O. 1994. A process model for friction welding of Al-Mg-Si alloys and Al-SiC metal matrix composites *Acta metall. mater.*, 42(5): 1595-1622.

10. Kang, C. Y., North, T. H., and Perovic, D. D. 1996. Microstructural features of friction welded MA 956 superalloy material. *Metall. and Mater. Trans.*, 27A(12): 4019–4029.

11. Kim, Y. C., Fuji, A. C, and North, T. H. 1995. Residual stress and plastic strain in AISI 304L titanium friction welds. *Mat. Sci. ad Tech.*, 11(4): 383–388.

12. Arzt, E., and Singer, R. F. 1984. The effect of grain shape on stress rupture of the oxide dispersion strengthened superalloy Inconel MA 600. *Proc. 5th Internat. Symp. on Superalloys*, AIME, Champion, Pa.

Appendix

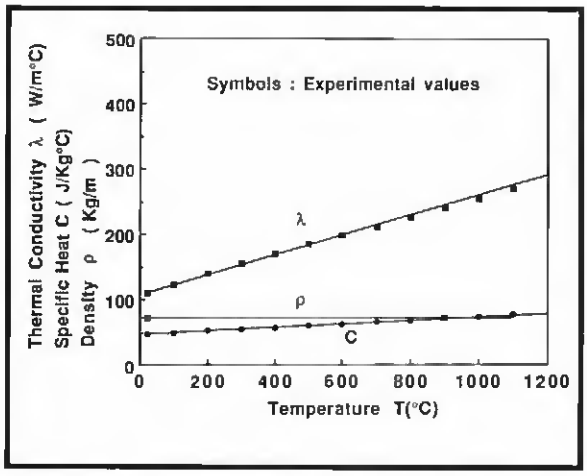

Fig. A1 — Thermal conductivity, specific heat and density of MA 956 superalloy base material at a range of temperatures.

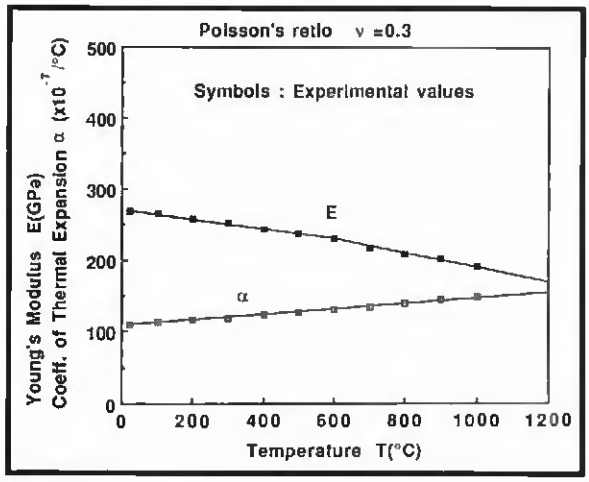

Fig. A2 — Young's modulus and coefficient of thermal expansion of MA 956 superalloy base material at a range of temperatures.

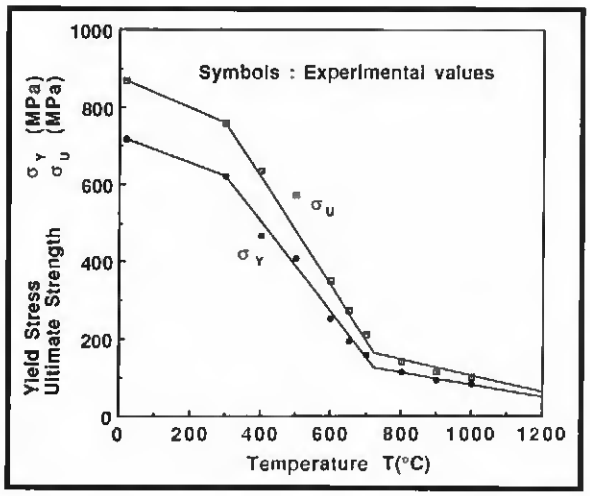

Fig. A3 — Yield strength and ultimate tensile strength of MA 956 superalloy base material at a range of temperatures.